NANO LETTERS
Cite This: Nano Lett. XXXX, XXX, XXX−XXX
Letter
pubs.acs.org/NanoLett

Anisotropic Flow Control and Gate Modulation of Hybrid Phonon-Polaritons

Francisco C. B. Maia,[*,†] Brian T. O'Callahan,[‡] Alisson R. Cadore,[§] Ingrid D. Barcelos,[†,§] Leonardo C. Campos,[§] Kenji Watanabe,[∥] Takashi Taniguchi,[∥] Christoph Deneke,[⊥,#] Alexey Belyanin,[○] Markus B. Raschke,[‡] and Raul O. Freitas[*,†]

[†]Brazilian Synchrotron Light Laboratory (LNLS), Brazilian Center for Research in Energy and Materials (CNPEM), 13083-970 Campinas, Sao Paulo, Brazil

[‡]Department of Physics, Department of Chemistry, and JILA, University of Colorado, Boulder, Colorado 80309, United States

[§]Department of Physics, Federal University of Minas Gerais, 30123-970 Belo Horizonte, Minas Gerais, Brazil

[∥]National Institute for Materials Science, Namiki 305-0044, Japan

[⊥]Brazilian Nanotechnology National Laboratory (LNNano), Brazilian Center for Research in Energy and Materials (CNPEM), 13083-970 Campinas, Sao Paulo, Brazil

[#]Applied Physics Department, Gleb Wataghin Physics Institute, University of Campinas (Unicamp), 13083-859 Campinas, Sao Paolo, Brazil

[○]Department of Physics & Astronomy, Texas A&M University, College Station, Texas 77843-4242, United States

Supporting Information

ABSTRACT: Light−matter interaction in two-dimensional photonic or phononic materials allows for the confinement and manipulation of free-space radiation at sub-wavelength scales. Most notably, the van der Waals heterostructure composed of graphene (G) and hexagonal boron nitride (hBN) provides for gate-tunable hybrid hyperbolic plasmon phonon-polaritons (HP^3). Here, we present the anisotropic flow control and gate-voltage modulation of HP^3 modes in G-hBN on an air−Au microstructured substrate. Using broadband infrared synchrotron radiation coupled to a scattering-type near-field optical microscope, we launch HP^3 waves in both hBN Reststrahlen bands and observe directional propagation across in-plane heterointerfaces created at the air−Au junction. The HP^3 hybridization is modulated by varying the gate voltage between graphene and Au. This modifies the coupling of continuum graphene plasmons with the discrete hBN hyperbolic phonon polaritons, which is described by an extended Fano model. This work represents the first demonstration of the control of polariton propagation, introducing a theoretical approach to describe the breaking of the reflection and transmission symmetry for HP^3 modes. Our findings augment the degree of control of polaritons in G-hBN and related hyperbolic metamaterial nanostructures, bringing new opportunities for on-chip nano-optics communication and computing.

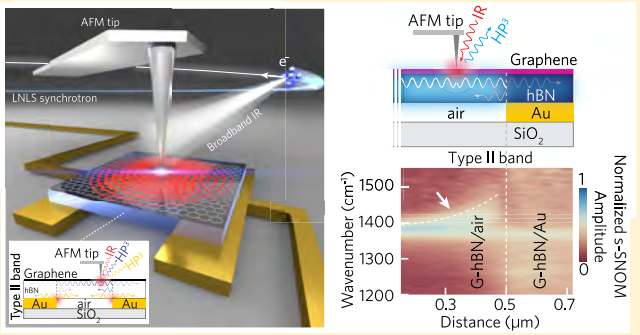

KEYWORDS: *Graphene/boron nitride, hybrid polaritons, nanophotonics, polaritonics, synchrotron infrared, near-field optics*

Photonics based on two-dimensional (2D) materials[1−5] exhibits a plethora of optical nanoscale phenomena, including the ability to confine free-space radiation to the deep sub-wavelength length scale.[6] Remarkably, photonic crystals and metamaterials built from hybrid 2D heterostructures provide for qualitatively new ways of light−matter interaction at the nanoscale[1,2] and are approaching their ultimate purpose as components for novel nanophotonic devices.[4,7,8] Nanoelectronics has recently reached a pivotal stage with the realization of atomically thin p−n junctions.[9]

Graphene has excelled at converting light into surface plasmon polaritons (SPPs)[10,11] with sub-diffraction wavelength gate tunability.[12,13] Similarly, mid-infrared free-space radiation can couple to sub-wavelength-confined hyperbolic phonon polaritons (HPhPs) in hBN[14−16] that are able to propagate up to 20 times the typical distances of graphene plasmons.[16] Merging the optical attributes of graphene and hBN, the G-hBN heterostructure constitutes an electromagnetic hybrid[2] with enhanced optoelectronic and photonic performances compared to its standalone constituents. In G-hBN, coupling

Received: September 14, 2018
Revised: January 19, 2019
Published: January 22, 2019

DOI: 10.1021/acs.nanolett.8b03732
Nano Lett. XXXX, XXX, XXX−XXX

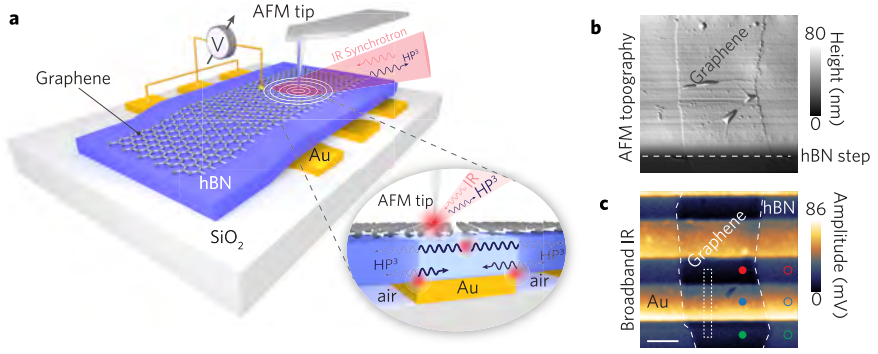

Figure 1. G-hBN polaritonic device architecture and tip-induced HP^3 mode excitation. (a) Schematic of the G-hBN heterostructure with SiO_2 and air-Au patterned (Au pads spaced by air gaps) substrates and electric gating. Using SINS, the metallic AFM tip launches the HP^3 modes and provides for nanoscale-resolved scattering detection. Inset: illustration of the asymmetric power flow for the HP^3 modes across G-hBN/(air−Au) junction. (b) AFM topography of hBN/SiO_2 edge region, hBN on Au pads, and graphene. (c) Corresponding broadband infrared near-field image with dielectric contrast of Au contacts under the 20 nm of hBN and the graphene sheet (scale bar: 1 μm). Circles indicate locations of near-field spectra shown in Figure 2. White dashed frame denotes the spectral line scan shown in Figure 3c.

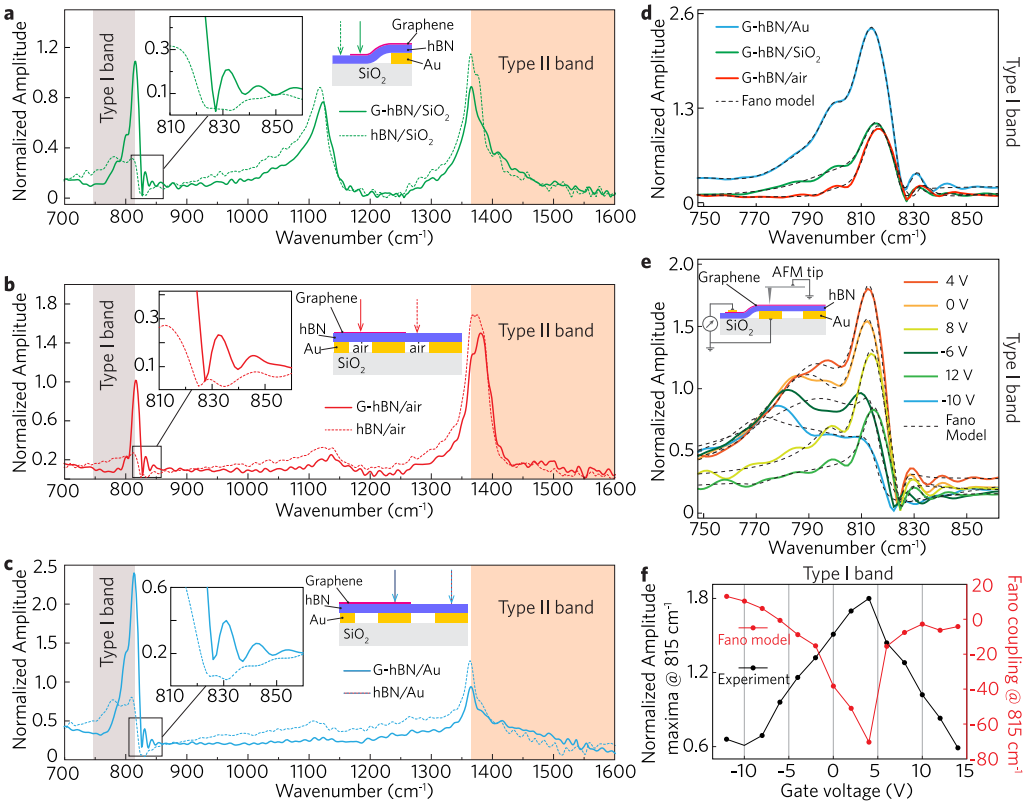

Figure 2. Substrate and gate tuning of the G-hBN HP^3 response. SINS point spectra of G-hBN and hBN on (a) SiO_2, (b) air (freestanding structure), and (c) Au, with measurement locations as indicated in the schematics (arrows) and type I (746 to 819 cm^{-1}) and type II (1370 to 1610 cm^{-1}) bands highlighted. Insets in panels a−c: zoomed-in panel showing spectral oscillations near the edge of the type I band associated with the graphene/hBN coupling. (d) Type I band optical response of the G-hBN on Au, SiO_2 and air, respectively, with characteristic Fano lineshapes and corresponding numerical fits (dashed black curves). (e) Gate tuning of the type I band response and device schematic for controlling gate bias between graphene and Au (inset). (f) Gate voltage dependence of normalized amplitude maxima (from spectra in panel e) and Fano coupling strength of the 815 cm^{-1} mode.

between graphene SPPs and in-plane polarized HPhPs of hBN has created gate-tunable hybrid hyperbolic plasmon phonon-polariton (HP^3) modes.[15,17] G-hBN not only supports graphene plasmons with reduced damping[18] but also HP^3s with propagation lengths up to 2 times greater than HPhPs in bare hBN,[17] with great potential for emission control driven by the surrounding media, as recently suggested theoretically.[19]

The rectification of phonons, often measured through thermal transport, has been predicted in the 1D chain of atoms with a mass gradient[20] and across interfaces between materials of different atomic masses[21] and has been reported in boron nitride nanotubes.[22] The asymmetry of reflection coefficients of graphene SPPs has been observed across grain boundaries due to a variation of the doping density and the SPP momentum.[23] To date, however, a G-hBN-based device

DOI: 10.1021/acs.nanolett.8b03732
Nano Lett. XXXX, XXX, XXX−XXX

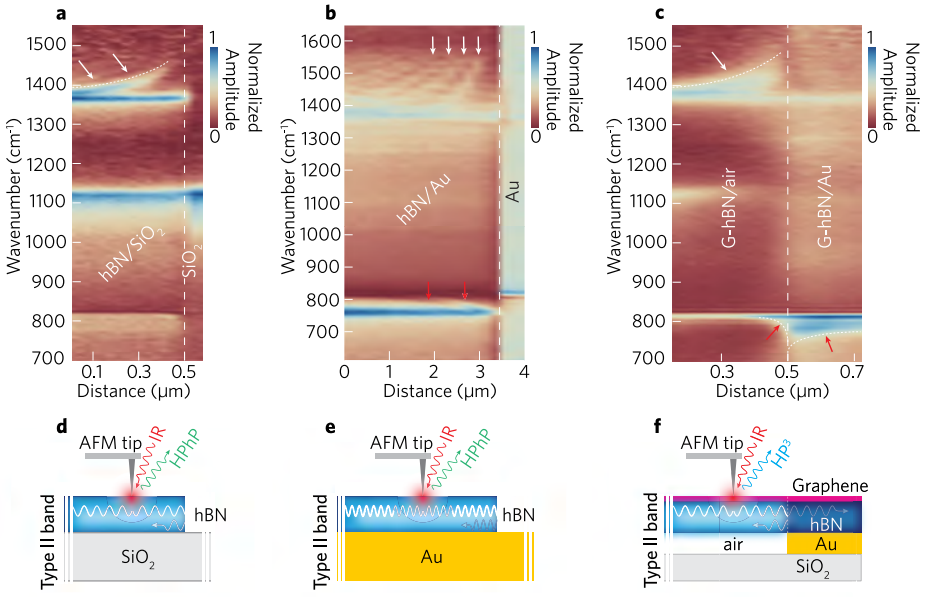

Figure 3. HPhP and HP^3 modes being reflected at the hBN crystal edge and at the G-hBN/(air−Au) junction. Spectral linescans near the edges of (a) a 20 nm thick hBN crystal on SiO_2 (hBN/SiO_2) and (b) a 240 nm thick hBN crystal on Au (hBN/Au). (c) Spectral linescan, for zero gate voltage, across G-hBN/(air−Au) with regions of amplitude depletion or increase for the type I (on Au side) and type II (on air side) modes, as indicated by arrows. (d−f) Schematics of polaritonic wave propagation, respectively, near the hBN/SiO_2, hBN/Au, and the junction. The SiO_2 surface phonon is seen at ∼1130 cm^{-1} in panels a and c.

able to regulate the flow of polariton waves and with full electro-optical control of the local polaritonic response is still elusive.

In this work, we demonstrate bias-control of the local response of out-of-plane polarized HP^3 modes. By configuring the G-hBN/Au heterostructure as a gate-controllable device (Figure 1a), we externally modulate the graphene plasmons and achieve fine-tuning of the optical response of the type I HP^3 mode (Figure 2). Regarding the propagation of the polaritons in the G-hBN, we primarily report asymmetric power flow of the in-plane HP^3 waves near the substrate air−Au transition, which is called G-hBN/(air−Au) junction (Figure 1a). These effects are probed by using scattering scanning near-field microscopy (s-SNOM), configured for synchrotron infrared nanospectroscopy (SINS; see the Methods section).[24−26] SINS provides for momentum matched excitation required for exciting polaritonic waves in G-hBN. In the article, the electric gate modulation is addressed first. In sequence, we present the anisotropic control of the HP^3 power flow, which is followed by our discussion on both effects.

Results. *Substrate Influence and Gate Control.* Figure 2a−c shows SINS amplitude spectra at different device locations as indicated schematically. The spectra in Figure 2a, taken on the hBN/SiO_2 region with and without graphene, are characterized by three resonances assigned to the type I band of hBN (746−819 cm^{-1}), SiO_2 surface phonon-polariton near 1130 cm^{-1}, and the hBN type II band (1370−1610 cm^{-1}).[17] Concerning the type II band, the comparison of hBN/SiO_2 and $G\text{-}hBN/SiO_2$ spectra (Figure 2a) reveals that graphene prompts a slight blue shift of the transverse optical (TO) response at 1365 cm^{-1}. For hBN/air and G-hBN/air (Figure 2b), however, the amplitude increases with respect to both SiO_2 (Figure 2a) and Au (Figure 2c). As shown in ref 27, type II HP^3 modes present higher momenta (higher confinement) over Au than over air or SiO_2. This explains the reduced amplitudes of the type II response over Au because launching highly confined HP^3 modes is expected to be less effective.[28]

In contrast, the type I band behaves distinctly. Figure 2a shows a HP^3 amplitude increase for type I band of more than a factor of 2 for $G\text{-}hBN/SiO_2$ in comparison with hBN/SiO_2, while previous reports[15,17] showed only a relative increase of less than 50%. The HP^3 amplitude increase also takes place for G-hBN/air with respect to hBN/air (Figure 2b). Figure 2c shows the amplitude of the type I modes for G-hBN/Au with distinct line-shape and almost a factor of 3 larger magnitude compared to hBN/Au. Comparatively, G-hBN/Au yields the largest amplitude increase, indicating that Au supports the HP^3 coupling (see the Supporting Information). The spectral oscillations outside the type I band (insets of Figure 2a−c) are a manifestation of pure SPP modes of graphene, which are seen only in the G-hBN heterostructure spectra. The interaction of broadband SPPs of graphene with HPhPs of hBN, resulting in amplitude changes and line-shape asymmetry, can be described by a Fano model (see the Supporting Information).[29−31] The analytic expression of the Fano resonance[32] $E_{Fano}(\omega)$, is given by:

$$E_{Fano}(\omega) \propto \frac{p(f\Gamma + (\omega - \omega_0))^2}{(\omega - \omega_0)^2 + \Gamma^2} \quad (1)$$

which is composed of the dimensionless Fano coupling f, excitation frequency ω, phonon frequency ω_0, damping Γ and the transition dipole strength of the coupled mode p. The Fano coupling f corresponds to the dipole strength of the transition between the discrete and continuum states. Thus, f provides a measure for the polaritonic coupling in the HP^3 modes. We extend the eq 1 to the case of interaction of multiple HPhPs modes (index j) with the graphene quasi-continuum SPPs, and a non-resonant background E_{nr} (see the Supporting Information), resulting in the complex expression:

DOI: 10.1021/acs.nanolett.8b03732
Nano Lett. XXXX, XXX, XXX−XXX

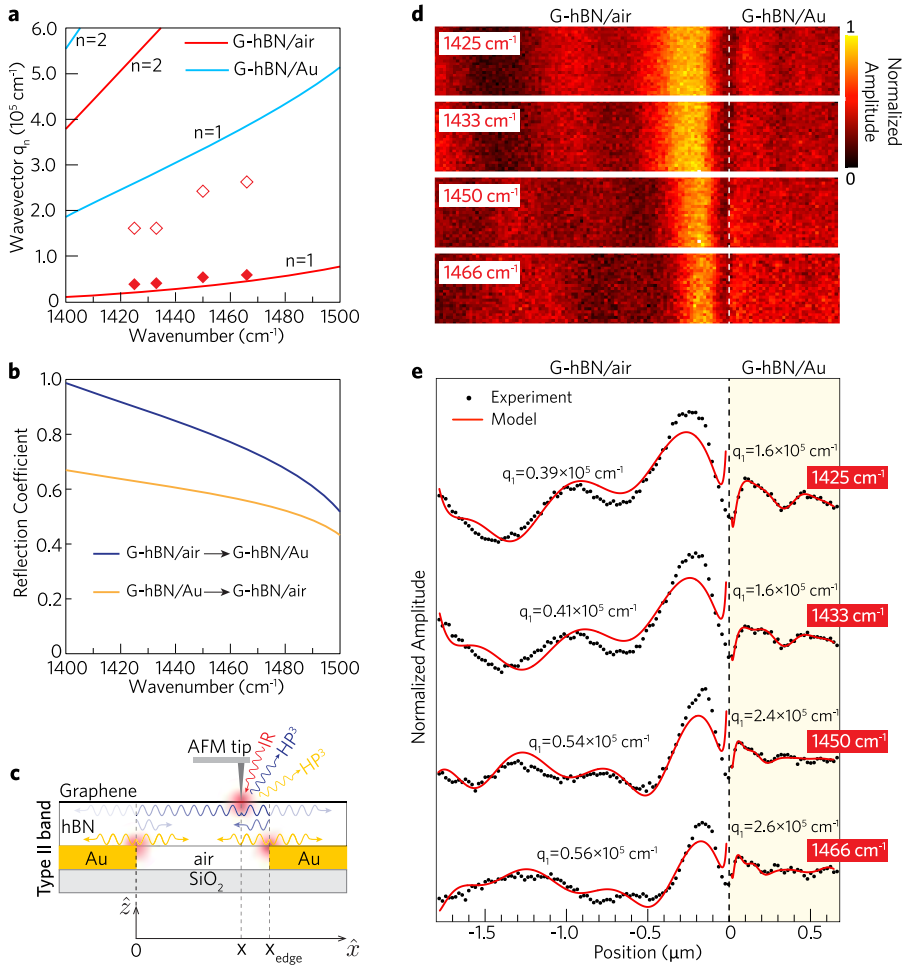

Figure 4. Frequency–momentum dispersion relation, calculated reflection coefficients for the type II HP^3 modes propagating over the G-hBN/(Au–air) junction, and narrow-band amplitude maps and amplitude profiles. (a) Calculated frequency–momentum dispersion relation of the type II HP^3 modes for Au (blue curves) and air (red curves) substrates for a measured 160 meV Fermi level of the graphene. hBN discrete polariton dispersion branches with momenta q_n are shown for n = 1 and 2 mode indices (see the Supporting Information). Model-extracted momentum for air (◆) and Au (◇) are plotted in panel a. (b) Calculated reflection coefficients from eq 3 for type II HP^3 modes propagating from G-hBN/air to G-hBN/Au regions (blue curve) and in the opposite direction (yellow curve). (c) Schematic of HP^3 waves launched by tip and Au edges: tip launches isotropically circular waves that travel to and reflect at the G-hBN/(air–Au) junctions. HP^3 waves are also excited by Au edges. (d) Amplitude narrow-band maps reconstructed from a hyperspectral image of a 35 nm thick G-hBN on a 0.5 μm × 2.5 μm region near the G-hBN/(air-Au), which is marked by the vertical white dashed line, for different excitation wavenumbers in the type II band and zero gate voltage. (e) Amplitude profiles extracted from the narrow-band amplitude maps in panel d. Dots are experimental data and red lines are fits from the model considering both the tip and the Au edges as launchers of HP^3 waves, as shown in the cartoon in panel c.

$$E_{HP^3}(\omega) \propto \sum_j \frac{\sqrt{p_j}(f_i\Gamma_j + (\omega - \omega_{0j}))}{(\omega - \omega_{0j}) + i\Gamma} + E_{nr} \quad (2)$$

We use eq 2 (see the Supporting Information) to fit the type I band of the G-hBN on the different media (Figure 2d). G-hBN/SiO_2 and G-hBN/air present f-values with similar magnitudes for the 815 cm^{-1} mode. A large negative f-value is found for the 815 cm^{-1} mode over G-hBN/Au (see the Supporting Information). This suggests a much weaker coupling for SiO_2 and air than for Au.

On the G-hBN/Au heterostructure, gate voltage variation (see scheme in the Figure 2e inset) leads to significant modulation of the type I band (Figure 2e), albeit causing negligible changes in the type II band. The stronger gate influence on the type I band stems from the maximized coupling between the gate electric field parallel to the polarization direction of the out-of-plane modes in the type I band. The coupling is then hindered for the type II band because the electric gate is perpendicular to the in-plane polarized modes. This interpretation is supported by numerical simulations of the field structure in a similar system of hBN/Au for both type I and II bands,[33] where the type I modes are mostly polarized in the out-of-plane direction and type II modes present a rather high polarization disorder. Figure 2e displays type I amplitude spectra for gate voltages from −12 to 12 V. From −12 to 0 V, the type I band increases globally. From 0 to 4 V, despite a continuous increase of the 815 cm^{-1} mode amplitude, an onset of amplitude attenuation occurs for the 770 and 800 cm^{-1} resonances. From 4 to 12 V, the 815 cm^{-1} mode amplitude decreases almost monotonically, while the other two modes gradually quench.

Amplitude and model-extracted f-values for the 815 cm^{-1} mode are plotted as a function of the gate voltage in the Figure 2f. Amplitude maximum coincides with the minimum value of f at 4 V. Negative f-values indicate higher weight of discrete

DOI: 10.1021/acs.nanolett.8b03732
Nano Lett. XXXX, XXX, XXX–XXX

states than of continuum states in Fano-like systems.[30] Accordingly, the 815 cm^{-1} mode experiences greater enhancement when the contribution of HPhPs surpasses that of the plasmons in the HP^3 coupling. However, as the voltage is tuned away from 4 V, f magnitude decreases, correlating to augmented contributions from graphene plasmons to attenuation of the type I band.

Anisotropic Control of the HP^3 Power Flow. Through the spectral linescans in Figure 3, we compare propagating HPhP modes near the edge of the hBN crystal on SiO_2 (Figure 3a) and on Au (Figure 3b) substrates, with the propagation of HP^3 modes near the G-hBN/(air−Au) junction (Figure 3c). Whereas the hBN/SiO_2 spectral linescan shows only modest features for the type I band, the type II band presents the spatio-spectral fringes (arrows in the Figure 3a), typically, assigned to HPhP standing waves formed between the tip and the crystal edges: tip launches circular waves that propagate to the crystal edges, wherein they are back-reflected to the tip (Figure 3d).[16,34] Similar reflection effect was recently reported for HPhPs waves near crystalline defects of a hBN flake.[35] The dense pattern of fringes in the type II band of the hBN/Au spectral linescan (white arrows in the Figure 3b) reveals such standing waves (Figure 3e). HPhPs propagation and reflection is also seen in the type I band of hBN/Au (see the Supporting Information and Figure 3b). Analogue effects emerge in the spectral linescan across the G-hBN/(air−Au) junction (Figure 3c). Near the junction, the amplitudes of the type I and II HP^3 modes show spatial fringes, respectively, on the Au (red arrow in Figure 3c) and air (white arrows in Figure 3c) sides. Such features are similar to the hBN/SiO_2 standing waves near the crystal edge. Thus, we attribute those amplitude spatial fringes in the linescan across G-hBN(air−Au) to reflection of HP^3 waves due to a dielectric discontinuity caused by the air−Au transition (Figure 3f).

For the type II modes, the dispersion relations of the first two branches[15−17,36−38] (mode indices n = 1 and 2; see the Supporting Information) for each substrate are plotted in Figure 4a. Type II HP^3 momenta are higher over the Au region compared to the air region. Hence, the structure of polariton modes in G-hBN/air is different from that in G-hBN/Au leading to a mismatch of momenta at the junction. It is then straightforward to see that a given transverse mode from a high-momentum (strong-confinement) region scatters with high efficiency into a set of transverse modes in a region with a lower confinement, which is the case of the in-plane polarized HP^3 modes propagating from the Au to the air side. Conversely, the same process originated from the opposite side is much less efficient.[39] This is verified by calculations of the reflection coefficient r (see the Supporting Information)[40] of type II HP^3 modes traveling from a region with q_n into a region q'_n given by

$$r = \frac{q'_1 - q_1}{q'_1 + q_1} \prod_{n=2}^{S} \frac{(1 - q_1/q'_n)(1 + q_1/q_n)}{(1 - q_1/q_n)(1 + q_1/q'_n)} \tag{3}$$

Calculation of r (Figure 4b) shows that polaritons traveling from a high- to a low-momentum region (Au to air case) couple more efficiently than for the opposite direction (air to Au case). This asymmetry is, experimentally, observed in the SINS narrow-band amplitude maps in Figure 4d. Those maps are obtained from a hyperspectral image acquired next to the G-hBN(air−Au) junction (for the type I band; see the Methods section and the Supporting Information). Patterns of maxima and minima, representing different structures of polariton modes for different ω values, rise over Au and air in between junctions (Figure 4e). Those amplitude oscillations originate from the interference of tip-launched circular waves (ξ_{Tip} field) and waves from the Au edges ($\xi_{Au\ edges}$ field).[14,18,23] The resulting optical field $\xi_{Opt} = \xi_{Tip} + \xi_{Au}$ accounts for the nontrivial behavior of those polariton waves that cannot be ascribed either to pure plane waves launched by Au edges or to only circular waves launched by the tip.[16,27,41] As an insight for future experiments, one can isolate edge and tip contributions by exploring the sensitivity of the edge launching efficiency to the incident light polarization. Tip and edges waves amplitudes are given, respectively, by

$$\xi_{Tip} = A\left(\frac{e^{-i\alpha_0}e^{i(q_1+ik_1)2x}}{\sqrt{2x}} + \frac{e^{-i\alpha_1}e^{i(-q_1+ik_1)2(x_{edge}-x)}}{\sqrt{x_{edge}-x}}\right) + Ce^{-in} \tag{4}$$

and

$$\xi_{Au\ edges} = B_0\left(\frac{e^{-i\beta_0}e^{i(q_1+ik_1)x}}{x} + B_1\frac{e^{-i\beta_1}e^{i(-q_1+ik_1)(x_{edge}-x)}}{x_{edge}-x}\right) \tag{5}$$

We model ξ_{Tip} (eq 4) as tip-launched circular waves, which decay geometrically as $1/\sqrt{d}$, where d is the distance from the source (tip apex).[18,41] These waves propagate toward the junctions at x = 0 and at $x = x_{edge}$, where they reflect and propagate back toward the tip at x (see Figure 4c). They carry the amplitude A and the phases α_1 and α_2. The term $Ce^{-i\eta}$ accounts for contributions from (i) a local dielectric near-field interaction between tip and sample, which does not depend on the tip position, and (ii) a nonresonant background originating from other scattering centers in the far-field illuminated confocal spot. $\xi_{Au\ edges}$ (eq 5) is defined by the counter-propagating waves launched by the Au edges, where (B_1,β_1) and (B_2,β_2) are the pairs of amplitude and phase, respectively, of waves emerging from the edges at x = 0 and at $x = x_{edge}$. We assume that the edge-launched waves decay as $1/d$ because we treat the edges as a linear series of point sources launching spherical waves inside the hBN crystal. This decay rate was successfully applied previously[18] for modeling plasmons waves launched by a graphene edge in a hBN-G-hBN system. Except for the different launchers efficiency and damping constants, the model proposed by Woessner *et al.*[18] inspired our modeling of polariton waves launched by multiple sources. Tip- and edge-launched waves have the same complex momentum, with q and κ representing real and imaginary parts, respectively (see the Supporting Information for more details).

We comment the differences of the $1/d$ geometrical decay of the edge launched waves, in our case, and recent observations of edge-launched plane waves by Yoxall *et al.*[42] and Ambrosio *et al.*[33], wherein a sample with the Au edge located atop the hBN crystal and a hBN crystal lying on the Au surface are, respectively, investigated. In those works,[33,42] thus, the launching edges and tip are directly exposed to the far-field illumination, whereas in our device, Au pads (and Au edges) are buried as shown in Figure 1a. The polaritons launching efficiency scales with the antenna efficiency on converting free-space radiation (far-field) into highly confined electric fields at edges or tip. Therefore, we cannot expect that our Au edges

DOI: 10.1021/acs.nanolett.8b03732
Nano Lett. XXXX, XXX, XXX−XXX

present the same efficiency reported in the referred works because, in our case, the illumination must transmit the graphene−hBN structure to access the Au edge. Accordingly, the polaritons launched at the bottom surface of the hBN must travel up to the top hBN surface to be tip-detected. In the past cases, polaritons are already launched at the top surface. Moreover, both Yoxall *et al.*[42] and Ambrosio *et al.*[33] report on HPhPs properties of hBN, while we focus on HP^3 in G-hBN heterostructures over the air−metal heterointerface. As previously shown, the hybridization with graphene plasmons, importantly, leads to hybrid waves with different properties[17] from the HPhPs ones.

The fits of the experimental amplitude profiles in Figure 4e, which are extracted from the narrow-band amplitude maps in Figure 4d, to the modeled amplitude ξ_{Opt} yield momenta and amplitudes of the polaritonic waves for each value of ω over air and Au regions. From the model-extracted amplitudes, we find that tip launching efficiency (σ)[41] is dominant regardless of substrate ($\sigma_{Tip} \gg \sigma_{Au\ edges}$; see the Supporting Information). Model-extracted momenta over air $q_{1,air}$ reasonably match the momentum-frequency dispersion relation calculations (Figure 4a). The predictions for Au substrate present larger $q_{1,Au}$ values than those determined by the fits (Figure 4a), likely because boundary conditions (see the Supporting Information) related to sample inhomogeneities were not included in the model, for simplicity. Nevertheless, the main trend of the systematic increase of $q_{1,Au}$ with ω follows the theoretical dispersion relations for the system (Figure 4a). Also, the fact that $q_{1,Au} \gg q_{1,air}$ confirms that the type II HP^3 modes are more confined (higher momenta values) over Au than in the air regions.[27] Therefore, air and Au differently modify the dielectric environment in the G-hBN heterostructure and, thus, determine HP^3 momenta. The model-extracted momenta give $q_{1,Au} \gg q_{1,air}$ indicating, according to the calculated reflection coefficients r (Figure 4b), lower reflection for HP^3 traveling in the Au-to-air direction rather than in the opposite direction. This configures an asymmetric regulation of HP^3 power flow across the dielectric junction.

Discussion and Conclusions. The gate control demonstrates the nature of the HP^3 coupling between the quasi-continuum SPPs of graphene interacting with discrete HPhPs of hBN. In particular, the combined tunability and anisotropic control of the HP^3 power flow can inspire future design of full polaritonic nanodevices in analogy to electronic transistors. Our results on anisotropic regulation of the power flow differs from optical isolation, as implemented in, e.g., Faraday isolators, because our experimental conditions do not break Lorentz reciprocity as our system is linear and time-independent and has no magnetic field applied.[39] In contrast, the anisotropic power flow control is a consequence of the local excitation of HP^3s with mode index $n = 1$, which can couple to higher order modes during transmission to regions of different polariton confinement. It is this difference in coupling which breaks the symmetry. However, the process is still reversible in the following sense, when the $n = 1$ tip-excited polaritons in region A experience the substrate dielectric junctions, they transmit into a superposition of polariton modes with mode indices $n \geq 1$ when propagating into region B. If that same superposition, with the same relative phase relation, is incident on the boundary from region B toward region A, it will combine to create a pure $n = 1$ transmitted mode propagating into region A. In summary, we present and quantitatively explain substrate-mediated anisotropic power flow and gate control of HP^3 out-of-plane modes in G-hBN heterostructures. Our observations provide for fine control of subdiffractional confined light, which is a prime step toward the realization of nanoscale on-chip polaritonic elements for optical communication and logic applications.

Methods. *Sample Preparation.* The G-hBN heterostructure was assembled onto SiO_2, Au stripes, and across air gaps by standard mechanical exfoliation using adhesive tape.[43,44] The flatness and quality of the hBN and graphene surfaces were characterized through a combination of optical microscopy, atomic force microscopy (AFM), and Raman spectroscopy. An electrode on top of the graphene region allowed for charge injection by tuning the gate voltage as illustrated (Figure 1a). The graphene is identified by the AFM topography (Figure 1b) and in the spectrally integrated broadband s-SNOM image (Figure 1c), with corresponding dielectric contrast from the underneath Au contacts. The combined AFM/s-SNOM imaging confirms that the 20 nm hBN crystal smoothly bridges the Au contacts, thus forming free-standing G-hBN/air regions. The Au stripes (60 nm thick) were designed by standard electron-beam lithography and thermal metal deposition. In sequence, single layer of mechanically exfoliated graphene was transferred atop of hBN flake forming the G-hBN/SiO_2, G-hBN/Au, and G-hBN/air heterostructures constructing the sample structure shown in Figure 1a. The graphene partially covered the flake leaving areas with bare hBN. After each material transference, the sample was submitted to thermal annealing at 350 °C with constant flow of Ar:H_2 (300:700 sccm) for 3.5 h to remove organic residues. Residues are likely to have contributed to the doping discussed in the Substrate Influence and Gate Control section. The heterostructures measured in the Figures 2 and 3a corresponded to a 20 nm thich hBN, while those in Figure 4 corresponded to a 35 nm thick crystal.

Synchrotron Infrared Nanospectroscopy Experiments. SINS, carried out at the Brazilian Synchrotron Light Laboratory (LNLS) provided for tip-based nanolocalized spectroscopy, imaging and spatio-spectral probing as established for graphene SPPs,[12,13,23] hBN HPhPs,[16,34] and G-hBN HP^3s.[15,17] In its implementation with synchrotron radiation, SINS operates with high spectral irradiance through the mid-IR range (700 to 3000 cm^{-1})[26] and it is capable of probing both hBN Reststrahlen bands simultaneously. In the infrared (IR) beamline of the LNLS, the infrared radiation extracted from a 1.67 T bending magnet is collimated and then coupled to a commercial s-SNOM (NeaSnom, Neaspec GmbH).[45] The IR synchrotron beam is focused on the metallic AFM tip shaft (NCPt-Arrow and PtSi-NCH, Nanoworld AG), which works as an extended antenna of about 25 nm apex radius. This antenna, which has a quasi-achromatic response in the mid-IR range, becomes an evanescent broadband source with dimensions comparable to the tip size. Operating in semi-contact mode AFM (tip frequencies from 250 to 350 kHz), the sample is brought in close proximity to the tip. The optical fields confined in the gap between tip apex and the sample gap generate an mutual polarization with amplitude and phase carrying the local sample dielectric response.[46] A mercury cadmium telluride detector (MCT KLD-0.1, Kolmar Technologies Inc.) is responsible for the detection of the scattered fields from the tip−sample interaction volume. For background suppression, we perform lock-in detection of the MCT signal on the second and third harmonics of the tip frequency.[47] Phase-sensitive nanospectroscopy is obtained by mounting the

DOI: 10.1021/acs.nanolett.8b03732
Nano Lett. XXXX, XXX, XXX−XXX

tip−sample stage in an asymmetric interferometric scheme, which is also used to demultiplex the spectral response of the broadband beam in similar fashion as Fourier Transform IR spectroscopy (FTIR).[48,49] We used 5 cm^{-1} spectral resolution by setting 2 mm optical path difference (OPD) of travel for the scanning mirror. The spectra acquisition was done by integrating over 2048 points with 20.1 ms integration time per point. All spectra are normalized by a reference spectrum acquired from a clean gold surface (100 nm thick Au sputtered on a silicon substrate). The images shown in Figure 1b,c were taken with 250 pixels × 250 pixels with a 15 ms integration time per pixel.

SINS Hyperspectral Map Data Processing. Narrow-band maps shown in Figure 4a were extracted from a full hyperspectral map (the 2D s-SNOM map in which every tip position contains a broadband IR spectrum) of a 0.5 μm × 2.5 μm area on G-hBN over the air−Au substrate transition. This area was segmented in 25 pixels × 125 pixels. Each spectrum in the hyperspectral map resulted from 5 averages over the Fourier transform of an interferogram acquired with 600 μm optical path difference length, yielding 16.6 cm^{-1} spectral resolution, divided in 400 points with 5.7 ms integration time per point. The narrow-band amplitude maps (Figure 4a) were obtained by extracting the amplitude of selected frequency from the spectrum of each pixel. We used the open-source data mining software Orange (https://orange.biolab.si) for frequency slicing the hyperspectral data cube.

■ ASSOCIATED CONTENT

Supporting Information

The Supporting Information is available free of charge on the ACS Publications website at DOI: 10.1021/acs.nanolett.8b03732.

Additional details on the Fano model, G-hBN on air and gold substrates, calculated dispersion relations and reflection coefficients, the hybridization of Au surface plasmons and type I band hBN hyperbolic phonon-polaritons, and models of HP^3 waves (PDF)

■ AUTHOR INFORMATION

Corresponding Authors

*E-mail: francisco.maia@lnls.br.
*E-mail: raul.freitas@lnls.br.

ORCID

Alisson R. Cadore: 0000-0003-1081-0915
Ingrid D. Barcelos: 0000-0002-5778-7161
Kenji Watanabe: 0000-0003-3701-8119
Christoph Deneke: 0000-0002-8556-386X
Markus B. Raschke: 0000-0003-2822-851X
Raul O. Freitas: 0000-0002-3285-5447

Author Contributions

C.D. together with F.C.B.M., I.D.B., A.R.C., and R.O.F initiated the research. F.C.B.M., I.D.B., and A.R.C. conceived the architecture of the device. F.C.B.M., I.D.B., A.R.C., and R.O.F. carried out the experiments. L.C.C., K.W., T.T., and M.B.R. supplied hBN crystals. R.O.F. performed post-experimental data analysis of the hyperspectral maps. M.B.R., A.B., and B.T.O.C. developed and interpreted the theoretical approach of polaritonic reflection. F.C.B.M developed the models for interpretation of the amplitude spectra (Fano Model) and the polaritonic oscillations. F.C.B.M., M.B.R., and R.O.F. prepared the manuscript. All authors took part in the interpretation of the phenomena.

Notes

The authors declare no competing financial interest.

■ ACKNOWLEDGMENTS

The authors thank the LNLS for providing beamtime to this project, LNNano for assistance in the device construction, and Lab Nanomateriais at UFMG for allowing the use of the atomic-layer transfer system. We thank Y. Petroff, J. Roque, and H. Westfahl for the in-depth discussions and for stimulating the research. Thiago M. Santos, Vinícius O. da Silva, and Neaspec GmbH are acknowledged for the technical assistance in the experiments. K.W. and T.T. acknowledge support from the Elemental Strategy Initiative conducted by the MEXT, Japan and JSPS KAKENHI grant no. JP15K21722. A.R.C, I.D.B., and L.C.C. appreciate the financial support from CAPES, Fapemig, CNPq, and INCT/Nanomateriais de Carbono. C.D. acknowledges financial support by CNPq. M.B.R. and A.B. acknowledges financial support through the AFOSR grant no. FA9550-17-1-0341. B.T.O. and M.B.R. acknowledge support from the U.S. Department of Energy, Office of Basic Sciences, Division of Material Sciences and Engineering, under award no. DE-SC0008807.

■ REFERENCES

(1) Koenderink, A. F.; Alu, A.; Polman, A. Nanophotonics: Shrinking Light-Based Technology. *Science* **2015**, *348* (6234), 516−521.
(2) Basov, D. N.; Fogler, M. M.; Garcia de Abajo, F. J. Polaritons in van Der Waals Materials. *Science* **2016**, *354* (6309), aag1992.
(3) Caldwell, J. D.; Vurgaftman, I.; Tischler, J. G. Mid-Infrared Nanophotonics: Probing Hyperbolic Polaritons. *Nat. Photonics* **2015**, *9* (10), 638−640.
(4) Xia, F.; Wang, H.; Xiao, D.; Dubey, M.; Ramasubramaniam, A. Two-Dimensional Material Nanophotonics. *Nat. Photonics* **2014**, *8* (12), 899−907.
(5) Caldwell, J. D.; Vurgaftman, I.; Tischler, J. G.; Glembocki, O. J.; Owrutsky, J. C.; Reinecke, T. L. Atomic-Scale Photonic Hybrids for Mid-Infrared and Terahertz Nanophotonics. *Nat. Nanotechnol.* **2016**, *11* (1), 9−15.
(6) Caldwell, J. D.; Kretinin, A. V.; Chen, Y.; Giannini, V.; Fogler, M. M.; Francescato, Y.; Ellis, C. T.; Tischler, J. G.; Woods, C. R.; Giles, A. J.; et al. Sub-Diffractional Volume-Confined Polaritons in the Natural Hyperbolic Material Hexagonal Boron Nitride. *Nat. Commun.* **2014**, *5* (1), 5221.
(7) Roy, T.; Tosun, M.; Kang, J. S.; Sachid, A. B.; Desai, S. B.; Hettick, M.; Hu, C. C.; Javey, A. Field-Effect Transistors Built from All Two-Dimensional Material Components. *ACS Nano* **2014**, *8* (6), 6259−6264.
(8) Barcelos, I. D.; Cadore, A. R.; Alencar, A. B.; Maia, F. C. B.; Mania, E.; Oliveira, R. F.; Bufon, C. C. B.; Malachias, Â.; Freitas, R. O.; Moreira, R. L.; et al. Infrared Fingerprints of Natural 2D Talc and Plasmon−Phonon Coupling in Graphene−Talc Heterostructures. *ACS Photonics* **2018**, *5* (5), 1912−1918.
(9) Lee, C.-H.; Lee, G.; van der Zande, A. M.; Chen, W.; Li, Y.; Han, M.; Cui, X.; Arefe, G.; Nuckolls, C.; Heinz, T. F.; et al. Atomically Thin p−n Junctions with van Der Waals Heterointerfaces. *Nat. Nanotechnol.* **2014**, *9* (9), 676−681.
(10) Politano, A.; Chiarello, G. Plasmon Modes in Graphene: Status and Prospect. *Nanoscale* **2014**, *6* (19), 10927−10940.
(11) García de Abajo, F. J. Graphene Plasmonics: Challenges and Opportunities. *ACS Photonics* **2014**, *1* (3), 135−152.
(12) Fei, Z.; Rodin, a. S.; Andreev, G. O.; Bao, W.; McLeod, a. S.; Wagner, M.; Zhang, L. M.; Zhao, Z.; Thiemens, M.; Dominguez, G.;

DOI: 10.1021/acs.nanolett.8b03732
Nano Lett. XXXX, XXX, XXX−XXX

et al. Gate-Tuning of Graphene Plasmons Revealed by Infrared Nano-Imaging. *Nature* **2012**, *487* (7405), 82−85.
(13) Chen, J.; Badioli, M.; Alonso-González, P.; Thongrattanasiri, S.; Huth, F.; Osmond, J.; Spasenović, M.; Centeno, A.; Pesquera, A.; Godignon, P. Optical Nano-Imaging of Gate-Tunable Graphene Plasmons. *Nature* **2012**, *487*, 77−81.
(14) Li, P.; Lewin, M.; Kretinin, A. V.; Caldwell, J. D.; Novoselov, K. S.; Taniguchi, T.; Watanabe, K.; Gaussmann, F.; Taubner, T. Hyperbolic Phonon-Polaritons in Boron Nitride for near-Field Optical Imaging and Focusing. *Nat. Commun.* **2015**, *6* (1), 7507.
(15) Barcelos, I. D.; Cadore, A. R.; Campos, L. C.; Malachias, A.; Watanabe, K.; Taniguchi, T.; Freitas, R. D. O.; Deneke, C.; Maia, F. C. B. Graphene/h-BN Plasmon−Phonon Coupling and Plasmon Delocalization Observed by Infrared Nano-Spectroscopy. *Nanoscale* **2015**, *7* (27), 11620−11625.
(16) Dai, S.; Fei, Z.; Ma, Q.; Rodin, A. S.; Wagner, M.; McLeod, A. S.; Liu, M. K.; Gannett, W.; Regan, W.; Watanabe, K. Tunable Phonon Polaritons in Atomically Thin van Der Waals Crystals of Boron Nitride. *Science (Washington, DC, U. S.)* **2014**, *343* (6175), 1125−1129.
(17) Dai, S.; Ma, Q.; Liu, M. K.; Andersen, T.; Fei, Z.; Goldflam, M. D.; Wagner, M.; Watanabe, K.; Taniguchi, T.; Thiemens, M.; et al. Graphene on Hexagonal Boron Nitride as a Tunable Hyperbolic Metamaterial. *Nat. Nanotechnol.* **2015**, *10* (8), 682−686.
(18) Woessner, A.; Lundeberg, M. B.; Gao, Y.; Principi, A.; Alonso-González, P.; Carrega, M.; Watanabe, K.; Taniguchi, T.; Vignale, G.; Polini, M.; et al. Highly Confined Low-Loss Plasmons in Graphene−Boron Nitride Heterostructures. *Nat. Mater.* **2015**, *14* (4), 421−425.
(19) Kumar, A.; Low, T.; Fung, K. H.; Avouris, P.; Fang, N. X. Tunable Light-Matter Interaction and the Role of Hyperbolicity in Graphene-Hbn System. *Nano Lett.* **2015**, *15* (5), 3172−3180.
(20) Yang, N.; Li, N.; Wang, L.; Li, B. Thermal Rectification and Negative Differential Thermal Resistance in Lattices with Mass Gradient. *Phys. Rev. B: Condens. Matter Mater. Phys.* **2007**, *76* (2), 1−4, DOI: 10.1103/PhysRevB.76.020301.
(21) Roberts, N. A.; Walker, D. G. Phonon Wave-Packet Simulations of Ar/Kr Interfaces for Thermal Rectification. *J. Appl. Phys.* **2010**, *108* (12), 123515.
(22) Chang, C. W.; Okawa, D.; Majumdar, A.; Zettl, A. Solid-State Thermal Rectifier. *Science* **2006**, *314* (5802), 1121.
(23) Gerber, J. A.; Berweger, S.; O'Callahan, B. T.; Raschke, M. B. Phase-Resolved Surface Plasmon Interferometry of Graphene. *Phys. Rev. Lett.* **2014**, *113* (5), 1−5.
(24) Hermann, P.; Hoehl, A.; Patoka, P.; Huth, F.; Rühl, E.; Ulm, G. Near-Field Imaging and Nano-Fourier-Transform Infrared Spectroscopy Using Broadband Synchrotron Radiation. *Opt. Express* **2013**, *21* (3), 2913−2919.
(25) Bechtel, H. A.; Muller, E. A.; Olmon, R. L.; Martin, M. C.; Raschke, M. B. Ultrabroadband Infrared Nanospectroscopic Imaging. *Proc. Natl. Acad. Sci. U. S. A.* **2014**, *111* (20), 7191−7196.
(26) Pollard, B.; Maia, F. C. B.; Raschke, M. B.; Freitas, R. O. Infrared Vibrational Nanospectroscopy by Self-Referenced Interferometry. *Nano Lett.* **2016**, *16* (1), 55−61.
(27) Duan, J.; Chen, R.; Li, J.; Jin, K.; Sun, Z.; Chen, J. Launching Phonon Polaritons by Natural Boron Nitride Wrinkles with Modifiable Dispersion by Dielectric Environments. *Adv. Mater.* **2017**, *29*, 1702494.
(28) Fei, Z.; Andreev, G. O.; Bao, W.; Zhang, L. M.; McLeod, A. S.; Wang, C.; Stewart, M. K.; Zhao, Z.; Dominguez, G.; Thiemens, M.; et al. Infrared Nanoscopy of Dirac Plasmons at the Graphene-SiO_2 Interface. *Nano Lett.* **2011**, *11* (11), 4701−4705.
(29) Fano, U. Effects of Configuration Interaction on Intensities and Phase Shifts. *Phys. Rev.* **1961**, *124* (6), 1866−1878.
(30) Tang, T.-T.; Zhang, Y.; Park, C.-H.; Geng, B.; Girit, C.; Hao, Z.; Martin, M. C.; Zettl, A.; Crommie, M. F.; Louie, S. G.; et al. A Tunable Phonon−Exciton Fano System in Bilayer Graphene. *Nat. Nanotechnol.* **2010**, *5* (1), 32−36.
(31) Li, Z.; Lui, C. H.; Cappelluti, E.; Benfatto, L.; Mak, K. F.; Carr, G. L.; Shan, J.; Heinz, T. F. Structure-Dependent Fano Resonances in the Infrared Spectra of Phonons in Few-Layer Graphene. *Phys. Rev. Lett.* **2012**, *108* (15), 1−5.
(32) Luk'yanchuk, B.; Zheludev, N. I.; Maier, S. a.; Halas, N. J.; Nordlander, P.; Giessen, H.; Chong, C. T. The Fano Resonance in Plasmonic Nanostructures and Metamaterials. *Nat. Mater.* **2010**, *9* (9), 707−715.
(33) Ambrosio, A.; Tamagnone, M.; Chaudhary, K.; Jauregui, L. A.; Kim, P.; Wilson, W. L.; Capasso, F. Selective Excitation and Imaging of Ultraslow Phonon Polaritons in Thin Hexagonal Boron Nitride Crystals. *Light: Sci. Appl.* **2018**, *7* (1), 1 DOI: 10.1038/s41377-018-0039-4.
(34) Shi, Z.; Bechtel, H. A.; Berweger, S.; Sun, Y.; Zeng, B.; Jin, C.; Chang, H.; Martin, M. C.; Raschke, M. B.; Wang, F. Amplitude- and Phase-Resolved Nanospectral Imaging of Phonon Polaritons in Hexagonal Boron Nitride. *ACS Photonics* **2015**, *2* (7), 790−796.
(35) Dai, S.; Tymchenko, M.; Xu, Z.-Q.; Tran, T. T.; Yang, Y.; Ma, Q.; Watanabe, K.; Taniguchi, T.; Jarillo-Herrero, P.; Aharonovich, I.; et al. Internal Nanostructure Diagnosis with Hyperbolic Phonon Polaritons in Hexagonal Boron Nitride. *Nano Lett.* **2018**, *18* (8), 5205−5210.
(36) Novotny, L.; Hecht, B. *Principles of Nano-Optics*; Cambridge University Press: Cambridge, U.K., 2012.
(37) He, Y.; He, S.; Gao, J.; Yang, X. Nanoscale Metamaterial Optical Waveguides with Ultrahigh Refractive Indices. *J. Opt. Soc. Am. B* **2012**, *29* (9), 2559.
(38) Poddubny, A.; Iorsh, I.; Belov, P.; Kivshar, Y. Hyperbolic Metamaterials. *Nat. Photonics* **2013**, *7* (12), 948−957.
(39) Jalas, D.; Petrov, A.; Eich, M.; Freude, W.; Fan, S.; Yu, Z.; Baets, R.; Popović, M.; Melloni, A.; Joannopoulos, J. D.; et al. What Is — and What Is Not — an Optical Isolator. *Nat. Photonics* **2013**, *7* (8), 579−582.
(40) Dragone, C. Scattering at Junction of Two Waveguides with Different Surface Impedances. *IEEE Trans. Microwave Theory Tech.* **1984**, *32* (10), 1319−1328.
(41) Dai, S.; Ma, Q.; Yang, Y.; Rosenfeld, J.; Goldflam, M. D.; McLeod, A.; Sun, Z.; Andersen, T. I.; Fei, Z.; Liu, M.; et al. Efficiency of Launching Highly Confined Polaritons by Infrared Light Incident on a Hyperbolic Material. *Nano Lett.* **2017**, *17* (9), 5285−5290.
(42) Yoxall, E.; Schnell, M.; Nikitin, A. Y.; Txoperena, O.; Woessner, A.; Lundeberg, M. B.; Casanova, F.; Hueso, L. E.; Koppens, F. H. L.; Hillenbrand, R. Direct Observation of Ultraslow Hyperbolic Polariton Propagation with Negative Phase Velocity. *Nat. Photonics* **2015**, *9* (9), 674−679.
(43) Cadore, A. R.; Mania, E.; Watanabe, K.; Taniguchi, T.; Lacerda, R. G.; Campos, L. C. Thermally Activated Hysteresis in High Quality Graphene/h -BN Devices. *Appl. Phys. Lett.* **2016**, *108* (23), 233101.
(44) Cadore, A. R.; Mania, E.; de Morais, E. A.; Watanabe, K.; Taniguchi, T.; Lacerda, R. G.; Campos, L. C. Metal-Graphene Heterojunction Modulation via H2 Interaction. *Appl. Phys. Lett.* **2016**, *109* (3), 033109.
(45) Freitas, R. O.; Deneke, C.; Maia, F. C. B.; Medeiros, H. G.; Moreno, T.; Dumas, P.; Petroff, Y.; Westfahl, H. Low-Aberration Beamline Optics for Synchrotron Infrared Nanospectroscopy. *Opt. Express* **2018**, *26* (9), 11238.
(46) Keilmann, F.; Hillenbrand, R. Near-Field Microscopy by Elastic Light Scattering from a Tip. *Philos. Trans. A. Math. Phys. Eng. Sci.* **2004**, *362* (1817), 787−805.
(47) Ocelic, N.; Huber, A.; Hillenbrand, R. Pseudoheterodyne Detection for Background-Free Near-Field Spectroscopy. *Appl. Phys. Lett.* **2006**, *89* (10), 3−6.
(48) Huth, F.; Govyadinov, A.; Amarie, S.; Nuansing, W.; Keilmann, F.; Hillenbrand, R. Nano-FTIR Absorption Spectroscopy of Molecular Fingerprints at 20 Nm Spatial Resolution. *Nano Lett.* **2012**, *12* (8), 3973−3978.
(49) Govyadinov, A. A.; Amenabar, I.; Huth, F.; Carney, P. S.; Hillenbrand, R. Quantitative Measurement of Local Infrared Absorption and Dielectric Function with Tip-Enhanced near-Field Microscopy. *J. Phys. Chem. Lett.* **2013**, *4* (9), 1526−1531.

DOI: 10.1021/acs.nanolett.8b03732
Nano Lett. XXXX, XXX, XXX−XXX